RESEARCH ARTICLE

ADVANCED FUNCTIONAL MATERIALS
www.afm-journal.de

Twisted Type-II Rashba Homobilayers: A Platform for Tunable Topological Moiré Flat Bands

*Xilong Xu, Haonan Wang, and Li Yang**

The recent discovery of topological flat bands in twisted transition metal dichalcogenide homobilayers and multilayer graphene has sparked significant research interest. Here, a new platform for realizing tunable topological moiré flat bands: twisted type-II Rashba homobilayers, is proposed. By maintaining centrosymmetry, the interplay between Rashba spin-orbit coupling and interlayer interactions generates an effective pseudo-antiferromagnetic field, opening a gap within the Dirac cone with non-zero Berry curvature. Using twisted BiTeI bilayers as an example, it is predicted that the emergence of flat topological bands with a remarkably narrow bandwidth (below 20 meV). Notably, the system undergoes a transition from a valley Hall insulator to a quantum spin Hall insulator as the twisting angle increases. This transition arises from a competition between the twisting-driven effective spin-orbit coupling and sublattice onsite energies presented in type-II Rashba moiré structures. The high tunability of Rashba materials in terms of the spin-orbit coupling strength, interlayer interaction, and twisting angle expands the range of materials suitable for functionalizing and manipulating correlated topological properties.

1. Introduction

The interplay between electronic topology and correlation gives rise to numerous exotic quantum phases,[1–6] such as the fractional quantum Hall (FQH) states in Landau levels.[7–12] Recently, fractional quantum anomalous Hall (QAH) effect in the absence of Landau levels has been observed in moiré systems such as twisted bilayer $MoTe_2$ ($tMoTe_2$) and multilayer graphene/hexagonal boron nitride moiré superlattices, spurring tremendous research interest.[13–21] In these systems, topological moiré flat bands play an essential role in harboring correlation-driven fractional states.[22–24] For example, in rhombohedral-stacked $MoTe_2$ moiré bilayers, the Kane-Mele flat bands have been theoretically predicted,[25,26] and integer QAH states as well as quantum spin Hall (QSH) states have also been observed at integer filling factors.[17] Hence discovering new structures harboring topological flat bands is crucial for realizing and understanding topological physics in many-electron systems.

The Rashba effect, generally existing in materials with strong spin-orbit coupling (SOC) and broken inversion symmetry, is capable of creating spin-polarized electron states in the absence of external magnetic fields.[27–30] This effect is characterized by a broken spin degeneracy, leading to quasiparticle bands with opposite spin textures that are momentum offset.[31,32] The remarkable tunability of the Rashba effect has enabled the observation of various well-known phenomena including the QAH effect, spin Hall effect, spin-charge conversion, and spin-torque in semiconductor devices.[27,31–33] Particularly, the Rashba-like bands are considered as a Dirac-cone surrounded by metallic states, indicating its promising potential for realizing topological states. However, its small effective mass and accompanying metallic state make it challenging to isolate those nontrivial bands and be measured via transport experiments to realize decisive topological properties.

In this study, we propose the twisted type-II Rashba structure as a promising platform for realizing and controlling flat bands with rich topological phases. Unlike conventional noncentrosymmetric Rashba materials, the type-II Rashba structure is centrosymmetric, which can be achieved by stacking two oppositely polarized layers. The combination of Rashba SOC and interlayer hopping creates a pseudo-antiferromagnetic field, which preserves time-reversal symmetry but induces an energy gap in the Dirac cone with nonvanishing Berry curvature. When the bilayer structure is further twisted, we find the topological Z_2 flat bands as well as QSH insulating states. Such QSH states feature the Kane-Mele model with an effective SOC induced by the moiré pseudo-Zeeman potential. A particularly intriguing observation is that the system undergoes a topological phase transition from the valley Hall (VH) phase to the QSH phase as the twist angle increases to 3.3°. This transition arises from the competition between the sublattice energy difference and the effective SOC. Given the tunability of the Rashba intensity, interlayer interaction, and twist angle, our work highlights the potential of Rashba

---

X. Xu, H. Wang, L. Yang
Department of Physics
Washington University in St. Louis
St. Louis, MO 63130, USA
E-mail: lyang@physics.wustl.edu

L. Yang
Institute of Materials Science and Engineering
Washington University in St. Louis
St. Louis, MO 63130, USA

The ORCID identification number(s) for the author(s) of this article can be found under https://doi.org/10.1002/adfm.202425454

DOI: 10.1002/adfm.202425454

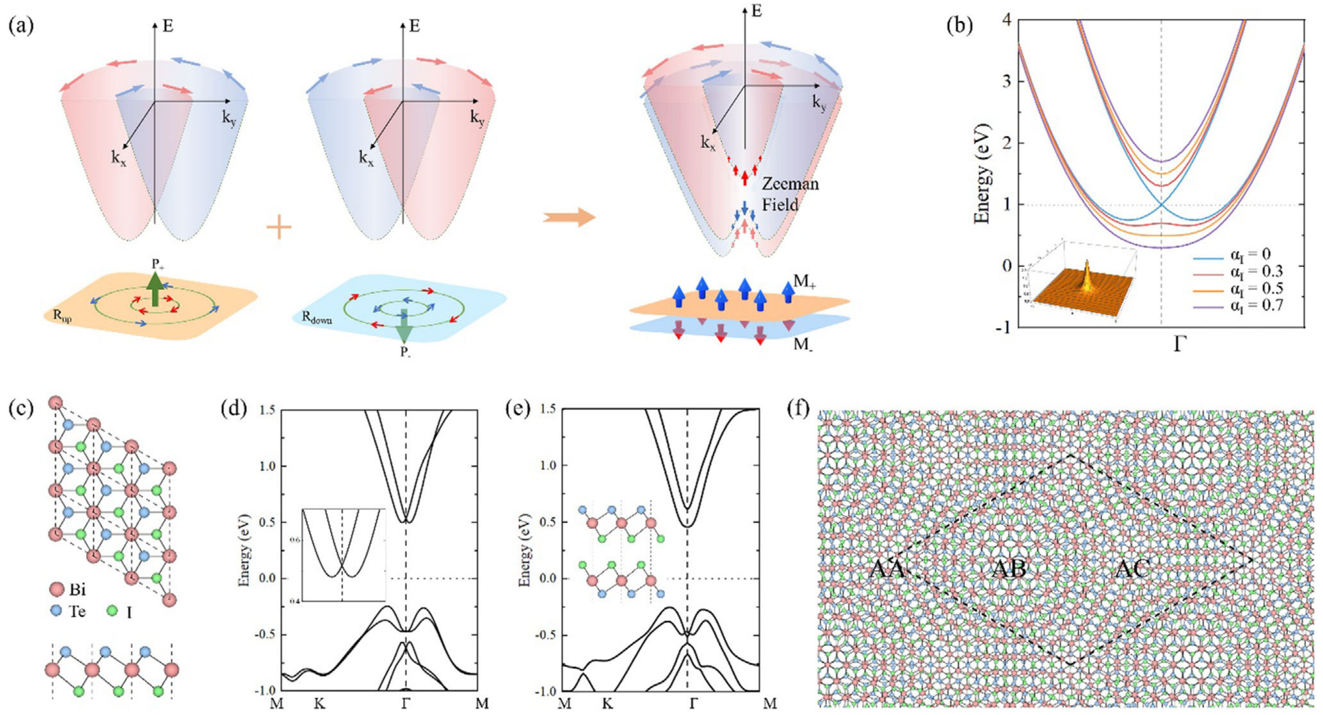

Figure 1. a) Schematic of type-II Rashba band structure and spin textures. b) Bands of a type-II Rashba bilayer with different interlayer couplings. The inset is the calculated berry curvature of the lowest-energy band around the Γ point. c) Crystal structures of monolayer BiTeI. d,e) Band structures of monolayer BiTeI and that of type-II Rashba bilayer. f) Top view of twisted bilayer BiTeI.

materials as a new family of material platforms for realizing and manipulating topological properties.

2. Result

2.1. Type-II Rashba Effect

Rashba effects are characterized by the two parabolic bands crossing over with spin polarizations in a helical texture, where the spin is oriented perpendicularly to the polar direction, as shown in the left panel of **Figure** 1a. The Rashba effect widely exists in materials with broken inversion symmetry. Interestingly, a newly proposed Rashba effect can also exist in centrosymmetric materials by stacking two identical layers with antiparallel polarization directions, which is referred to as the type-II Rashba effect (the right panel of Figure 1a).[32,34,35] To date various type-II Rashba materials have been successfully fabricated, and they are considered as a key ingredient in the next generation of spin field-effect transistors.[34,36,37] To capture the features of a type-II Rashba bilayer structure, a minimized Hamiltonian can be written as (see Text S1, Supporting Information)

$$\begin{aligned} H(\boldsymbol{k}) &= \frac{\hbar^2k^2}{2m^*}\zeta_0 + \alpha_R\zeta_z\left(k_xs_y - k_ys_x\right) + \alpha_I\zeta_xs_0 \\ &= \begin{pmatrix} \frac{\hbar^2k^2}{2m^*}+\alpha_R\left(k_xs_y-k_ys_x\right) & \alpha_Is_0 \\ \alpha_Is_0 & \frac{\hbar^2k^2}{2m^*}-\alpha_R\left(k_xs_y-k_ys_x\right)\end{pmatrix} \end{aligned} \tag{1}$$

where ζ and s are Pauli matrices that represent the layer pseudospins and spins, respectively. The off-diagonal block matrices stand for interlayer hopping. m^* and α_R denote the effective mass and Rashba SOC strength, respectively, and α_I is the strength of interlayer hopping. Because the interlayer hopping conserves spin, this Hamiltonian preserves the time-reversal symmetry, satisfying $TH(\boldsymbol{k})\,T^{-1} = H(-\,\boldsymbol{k})$, where $T = i\zeta_0s_y\mathcal{K}$ and $\mathcal{K}$ denotes the complex conjugation operator. Moreover, it also preserves the inversion symmetry $PH(\boldsymbol{k})\,P^{-1} = H(-\,\boldsymbol{k})$, where $P = \zeta_x\,s_0$. As a result, all bands exhibit double degeneracy in type-II Rashba materials, and the Berry curvature for the Kramers' degenerate pairs is vanishing. However, the Berry curvature for each band in the Kramers' pairs would remain nonzero. To see this, a unitary transformation, $U = \frac{1}{\sqrt{2}}\left(\zeta_0s_0 - i\zeta_ys_z\right)$, can be performed on the Hamiltonian, leading to

$$H_2(\boldsymbol{k}) = UH(\boldsymbol{k})\;U^{\dagger} = \frac{\hbar^2k^2}{2m^*} + \zeta_z\left(\alpha_R(k_xs_y - k_ys_x) + \alpha_Is_z\right) \tag{2}$$

where the second term essentially describes two 2D massive Dirac fermions. At $\boldsymbol{k} = 0$, a bandgap with $2\alpha_I$ is induced by the interlayer hopping term $\alpha_I\zeta_zs_z$ which can be regarded as a pseudo-antiferromagnetic field, as illustrated in the right panel of Figure 1a. Consequently, each band carries nonvanishing Berry curvature with a Berry phase of π, and the in-plane Rashba spin texture around the Dirac cone is switched in the out-of-plane direction. Moreover, the Dirac-cone bandgap increases as the interlayer hopping (α_I) increases, as depicted in Figure 1b. It is important to note that within a certain range of interlayer interaction strength, the bottom band becomes flat. This will help the formation of flat bands in twisted structures, as will be discussed in the following.

2.2. Twisted Type-II Rashba Homobilayer

The nonzero Berry curvature indicates the presence of topological states in type-II Rashba structures. However, these states are concealed within the Kramers' pairs due to the *PT* symmetry. Furthermore, the existence of parabolic bands results in metallic states within the Dirac-cone bandgap, thereby impeding the probing of topological states. To break the combined *PT* symmetry and gap out these metallic states, a weak periodic potential can be achieved by twisting the type-II Rashba homobilayers. This motivates our search for vdW materials with strong Rashba effects and interlayer interactions.

BiTeI is a layered vdW material with an out-of-plane polarization and a strong Rashba effect.[38–40] It has been fabricated and exfoliated and exhibits a large bulk photovoltaic effect.[41–44] As shown in Figure 1c, its monolayer structure consists of triple sublayers, similar to the *T*-phase of transition metal dichalcogenides (TMDs). The band structure of monolayer BiTeI is plotted in Figure 1d. Notably, the bottom two conduction bands exhibit a typical Rashba band splitting around the Γ point, while the top valence bands are more hybridized by different atomic orbitals that obscure the feature of Rashba splitting. Therefore, we mainly focus on the bottom two conduction bands around the Γ point in the following. These two conduction bands can be described by $H = \frac{\hbar^2 k^2}{2m^*} + \alpha_R(k_x s_y - k_y s_x)$ with an effective mass $m^* = 0.49\ m_e$ and Rashba strength $\alpha_R = 1.53$ eV Å, which is similar with those typical Rashba materials, such as GeTe (≈2.5 eV Å).[45] This significant Rashba effect is from the heavy-element compositions as well as the strongly broken inversion symmetry.

To construct the type-II Rashba structure, two oppositely polarized BiTeI monolayers are stacked. Depending on the interfacial atoms, there are two basic types of interfaces: Te–Te and I–I. We will discuss the I–I interface in the main manuscript, which is shown in the inset of Figure 1e. The Te–Te interface yields similar results, and the details are provided in the Supplementary Information. The band structure of bilayer BiTeI is presented in Figure 1e. As expected, the Dirac cone is now gapped due to interlayer hopping, forming a pair of parabolic-like energy dispersions. Each band is doubly degenerate due to the *PT* symmetry. This agrees well with our model Hamiltonian Equations (1) and (2) and Figure 1b. As we twist the homobilayer BiTeI at a commensurate small twist angle to form moiré superlattices, the local interlayer atomic displacement will go through a slow periodic modulation that allows various local atomic stackings in the moiré unit cell. Because of the three-fold rotational symmetry, there are three high-symmetry stackings, i.e., AA, AB, and AC, in the moiré unit cell. All three high-symmetry stackings feature a similar type-II Rashba band structure but with different Dirac-cone gaps due to their different interlayer interactions. (See Table S1, Supporting Information)

To capture the moiré modulations on interlayer interactions, the effective moiré Hamiltonian of the four lowest-energy conduction bands can be written as:[22,25,26]

$$H_{\text{Moiré}}\ (r,k) = \left(\frac{\hbar^2 k^2}{2m^*} + \Delta\ (r)\right) + \zeta_z\ \left(\alpha_R(k_x s_y - k_y s_x) + \alpha_I\ (r)\ s_z\right) \tag{3}$$

where the interlayer hopping now becomes as a periodic function and the term $\alpha_I(r)\zeta_z s_z$ contributes to a pair of opposite Zeeman moiré potentials. With the three-fold rotational symmetry, $\alpha_I(r)$ can be expanded as $\alpha_I\ (r) = M_0 + M_1 \sum_{j=1,3,5} \cos(G_j \cdot r + \psi)$, where $G_j = \frac{8\pi \sin(\frac{\theta}{2})}{\sqrt{3}a_0}\ (\cos(\frac{j-1}{3})\pi, \sin(\frac{j-1}{3})\pi)$ denotes the three moiré reciprocal lattice vectors, θ and $a_0 = 3.8$ Å denote the twist angle and lattice constant of the unit cell of BiTeI, respectively. Besides, $\Delta\ (r) = V_0 + V_1 \sum_{j=1,3,5} \cos(G_j \cdot r + \phi)$ stands for the scalar moiré potential that originates from modulation on the conduction band minimum over the moiré period. All the parameters in $\alpha_I(r)$ and $\Delta(r)$ can be determined from first-principles simulations of three high-symmetry stackings, as listed in Table S1 of SI.

The moiré band structures can be calculated by the plane-wave expansion. **Figure 2** plots moiré bands at three typical twist angles. One can clearly see that the Kramer pairs are formed at the time-reversal invariant momenta. This is because the moiré Hamiltonian Equation (3) still preserves the time-reversal symmetry, as required by the type-II Rashba structure. However, the moiré bands are now lifted at the moiré Brillouin zone corner, indicating that the twisted BiTeI homobilayer breaks the inversion symmetry for the moiré superlattices. This is because these AA, AB, and AC stackings have different electron affinities, as shown in Supporting Information, and are reflected by the nonzero value for ϕ in the moiré potential $\Delta(r)$. Moreover, within a small twist angle θ such as 3.5°, isolated flat bands are observed (C_1-C_4) with bandwidth ≈7 meV. This is substantially narrower than those calculated in twisted TMDs. For example, it is ≈20 or 40 meV for twisted $MoTe_2$ or WSe_2.[46] Figure 2e summarizes the evolution of the bandwidth with the twist angle. Such exceptional and tunable flatness indicates that twisted type-II Rashba structures can be a promising platform to realize and control many electron correlation effects.

2.3. Topological Phase Transition

Then we study the topological properties of these isolated flat (C_1-C_4) bands. Notice that as the twist angle increases, valleys are formed at the +K/-K point of the moiré Brillouin zone as presented in Figure 2. Moreover, Figure 2f shows that significant Berry curvature with equal values but opposite signs is distributed at the +K and -K points. Our berry curvature calculation further quantifies that the valley Chern number for the C_1 and C_2 (C_3 and C_4) bands is +1 (−1), featuring the valley Hall (VH) insulating states for twisted type-II Rashba BiTeI bilayers, which have been predicted and observed in non-twisted TMDs.[47,48] It is worth mentioning that even a relatively small pseudo-gap still allows for the characterization and verification of valley-related properties. For instance, nonlocal electrical measurements[49,50] or detecting spin Hall conductivity through the magneto-optical

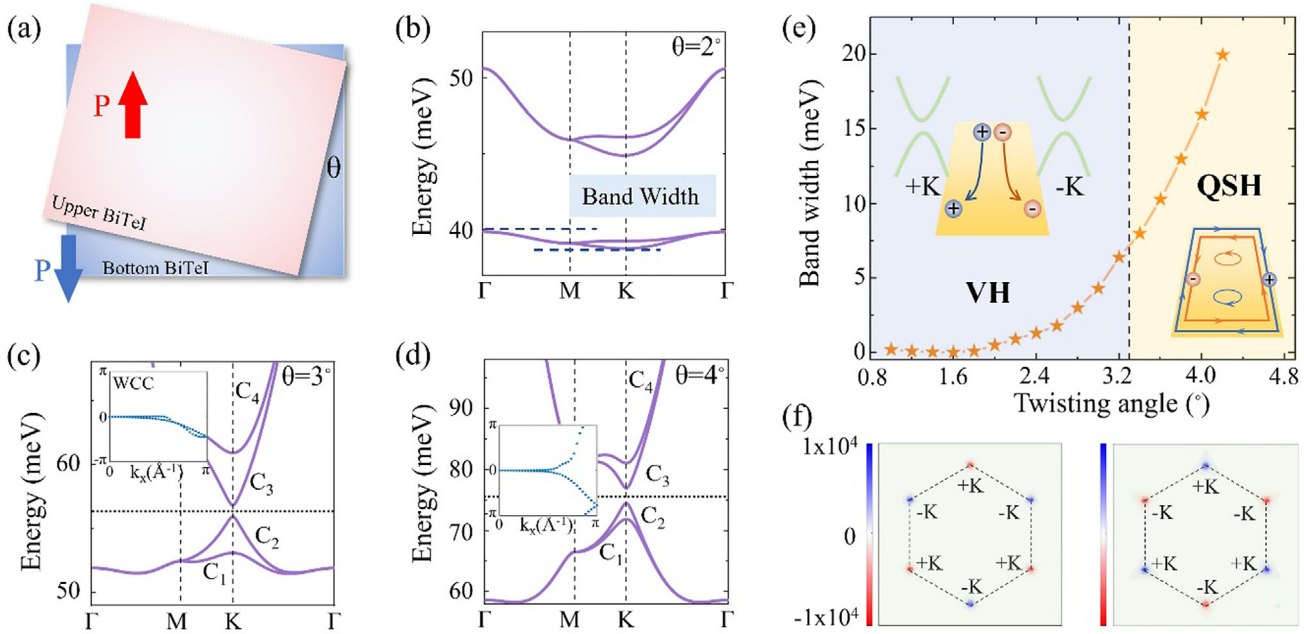

Figure 2. a) Schematic of Twisting bilayer BiTeI. Moiré bands with a twisting angle of 2° b), 3° c) and 4° d). The insets in (c) and (d) illustrate the evolution of the Wannier charge center. e) Variation of the bandwidth as a function of the twisting angle. The insets in (e) illustrate the different topological states in twisting bilayer BiTeI. f) Berry curvature of the two lowest conduction bands with a twisting angle of 3° and 4°, respectively.

Kerr effect (MOKE)[51] or spin pumping and inverse spin Hall effect measurements method[52] can be employed to indirectly confirm the presence of the valley Hall effect.

Importantly, we find a critical twist angle 3.3° where the bandgap between the C_2 and C_3 bands closes and forms a gapless Dirac cone. The Berry curvatures for the C_2 and C_3 bands reverse their signs, as shown in Figure 2f, suggesting a band inversion and topological phase transition. Because the twisted bilayer type-II Rashba BiTeI still preserves the time-reversal symmetry, its topology is characterized by the topological invariant Z_2, which can be calculated by the Wilson loop method that tracks the evolution of the Wannier charge center (WCC). As the twist angle becomes larger than the critical angle, the Z_2 topological invariant switches from 0 to 1 for the C_1 and C_2 bands, yielding a nontrivial topological insulating state when the C_1 and C_2 bands are filled.[53,54]

3. Discussion

Next, we have conducted an in-depth study to understand the reasons behind this topological transition. First, we find that in the VH insulating phase, the real-space wave functions of C_1 and C_2 bands at the +K/-K point are localized around the AC sublattice, while those of C_3 and C_4 bands are mostly localized around the AB sublattices (see Figure S2, Supporting Information). Such a sublattice energy splitting contributes to a term proportional to σ_z, where σ_z is a Pauli matrix that denotes the on-site energy difference of AC and AB sublattices.

Second, the expectation value of the spin operator, namely, $\langle \psi_n(k)|s_z|\psi_n(k)\rangle$ exhibits the opposite sign for each set of bands, as illustrated in **Figure** 3a, while the expectation value of $s_{x,y}$ is almost vanishing over the moiré Brillouin zone, indicating the spin texture of the low energy moiré bands is along the out-of-plane direction. Our simulation shows that, at the +K point, spins are ↓/↑ for the C_1/C_2 band located at the AC sublattice, and ↑/↓ for the C_3/C_4 band located at the AB sublattice. Such a spin splitting indicates that the spins are coupled with sublattices by a term $\sigma_z s_z$. Moreover, at the -K point, spins for each band are reversed, namely, ↑/↓ for the C_1/C_2 band at the AC sublattice, and ↓/↑ for the C_3/C_4 band at the AB sublattice, which can be described by a $-\sigma_z s_z$ term. In this sense, these states near the bandgap can be captured by a phenomenological model,[55,56]

$$H = \Delta\sigma_z + \lambda\tau_z\sigma_z s_z \tag{4}$$

where τ_z denotes the valley index. This model preserves the time-reversal symmetry but breaks the inversion symmetry due to the first term. The second term is indeed the effective intrinsic SOC term that features the Kane–Mele model, and it results in the quantum spin Hall (QSH) insulating states of the twisted type-II Rashba systems.

Finally, we reveal that how the terms in the Kane-Mele model in Equation (4) are harbored in the moiré Hamiltonian of Equation (3). Because of flat bandwidth, we can neglect the kinetic energy term and reduce Equation (3) to $H_{\text{Moiré}}(r,k) = \Delta(r) + \zeta_z\left(\alpha_R(k_x s_y - k_y s_x) + \alpha_I(r)\, s_z\right)$. Furthermore, around the critical bandgap closing at the $\pm K$ point, the spin texture is along the out-of-plane (z) direction, and the Rashba term approaches zero. Thus, only two terms of the moiré Hamiltonian are important, $\Delta(r) + \zeta_z\alpha_I(r)s_z$. Note that the scalar moiré potential $\Delta(r)$ of the twisted type-II Rashba BiTeI bilayer has two potential minimums around AB and AC stackings, which are ≈100 meV lower than that of the AA stacking, as shown in Figure 3b. In this scenario, this scalar moiré potential gives rise to Dirac-like bands

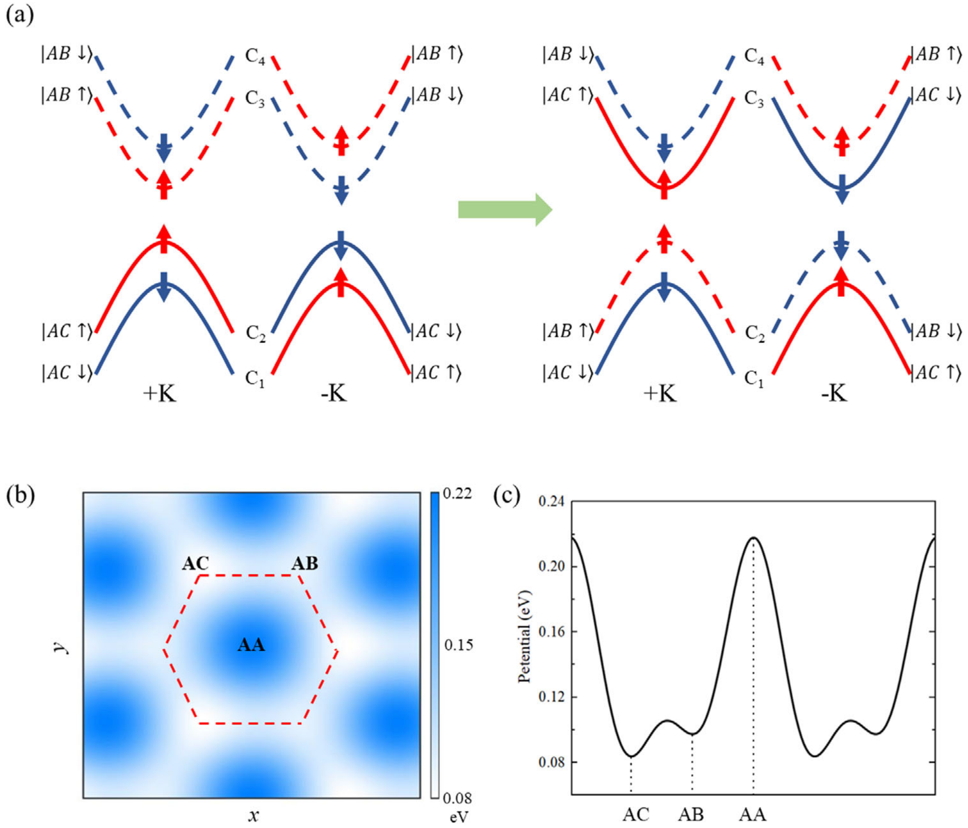

Figure 3. a) Schematic plots of bands before and after the topological phase transition. The arrow on each band denotes the spin orientation. b,c) Top and side views of the moiré potential of twisting bilayer BiTeI, respectively.

at the moiré Brillouin zone corner as well as a honeycomb lattice with AB and AC being two sublattices, which is illustrated in Figure 3b. Moreover, there is a tiny energy difference between AB and AC sublattices ≈13 meV, as shown in Figure 3c. Such a scalar moiré potential $\Delta(r)$ opens a trivial moiré bandgap at the moiré Brillouin zone corner and results in a $\Delta\sigma_z$ term. Similarly, the interlayer interaction $\alpha_I(r)$ can also form a moiré bandgap by with an extra prefactor, which is characterized by $\zeta_z\sigma_z$. Thus, the moiré Hamiltonian around the $\pm K$ point is essentially $\sigma_z + \zeta_z\sigma_z s_z$.

Notably, the layer pseudospins ζ_z in the Hamiltonian Equation (3) couple with both momentum and s_z, when a gap is open at k, a gap with an opposite sign has to open at $-k$. Hence the layer pseudospins ζ_z play a similar role with the valley pseudospins τ_z. There, the interlayer interaction $\alpha_I(r)$ works as an effective SOC. In this sense, the moiré Hamiltonian Equation (3) essentially harbors the Kane–Mele model (Equation (4)).

Generally, the SOC interaction is dependent on the gradient of the potential. The existence of effective SOC has also been demonstrated in other moiré systems, and it was revealed to be dependent on the gradient of moiré potential.[57,58] As the twist angle increases, the moiré period decreases, and the gradient of moiré potential increases. Consequently, the effective SOC strength dominates the gap over the sublattice energy difference for larger twist angles, driving the system into the QSH state. The QSH state can transition into a QAH state upon breaking time-reversal symmetry.[59,60] Furthermore, based on the intrinsic flat bands, the intrinsic magnetism may be spontaneously emerged upon electron doping, which could not only lead to the coexistence of the QSH and QAH phases, but may even give rise to a fractional quantum anomalous (FQAH) phase.[14,24,61]

Finally, the phase diagrams according to the Rashba effect and interlayer interaction are plotted. In **Figure** 4a, we show the topological phases between the C_2 and C_3 bands as a function of the twist angle (θ) and Rashba strength (α_R). We restricted the angles ranging from 1 degree to 8 degrees to maintain result accuracy. It is evident that VH and QSH states exist with a significant parameter range. This demonstrates that the observed topological phase transition as increasing twist angle is not incidental but rather intrinsic and robust. Moreover, when the Rashba strength reduces to ≈0.3, the system cannot achieve a topological state within our considered angel range, indicating the importance of the Rashba effect for the form of topological states.

Figure 4b presents the coordinative contributions from interlayer interaction and Rashba strength to the insulating QSH state. As mentioned at the beginning, a challenge to realize topological states is to isolate the nontrivial bandgap from the surrounding metallic states in Rashba materials. As seen from Figure 2b–d, the band energy at the K point needs to be higher than that at the Γ point to result in a finite gap. Figure 4b plots this energy difference and shows that larger interlayer interaction

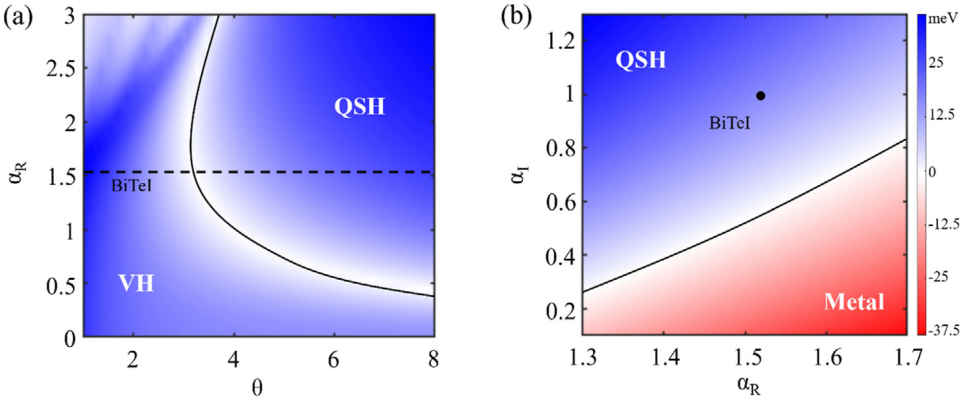

Figure 4. a) Phase diagram with the twist angle and Rashba parameter. b) That with the strength of Rashba parameter and interlayer interaction. The dashed line represents the parameter used in twist bilayer BiTeI. The solid line represents the critical phase transition boundary.

α_I and Rashba α_R will lift the K-point energy and favor insulating states. This also agrees with Figure 1b, in which the larger α_I and α_R lower the band energy at the Γ point. Finally, we observe that α_R and α_I increase linearly when the topological phase transition is satisfied, indicating that these two parameters need to be synchronized.

4. Conclusion

We have established the mechanism wherein inversion-stacked Rashba materials can undergo topological phase transitions under twisting. The essential ingredient is a type-II Rashba moiré system described at low energy by the universal Hamiltonian, Equation (1). The interplay between Rashba SOC and interlayer hopping generates a pseudo-antiferromagnetic field, maintaining time-reversal symmetry while opening an energy gap in the Dirac cone with nonzero Berry curvature. Upon twisting the bilayer, we observe topological Z_2 flat bands and QSH insulating states, described by the Kane–Mele model with effective SOC from the moiré pseudo-Zeeman potential. Notably, the system exhibits a topological phase transition from the VH phase to the QSH phase at a twist angle of 3.3°, driven by competition between the sublattice energy difference and effective SOC. This theoretical framework can potentially be realized using a wide range of materials as consistent layers. Potential candidates include polar structure (e.g., BiTeCl, Sb_2TeSe_2, TiNCl), IV-VI materials (e.g., blue-phosphorene-phase GeTe, SnTe, square buckled-phase PbS),[62,63] 2D ferroelectric materials (e.g., In_2Se_3), even some non-vdW Rashba materials (e.g., $BaCdK_2Sb_2$, KSnAs) via interface engineering.[45] These classic Rashba materials are expected to undergo topological phase transitions driven by appropriate interlayer interactions and moiré potential, and they can be easily manipulated by external conditions such as stress or electric fields. Furthermore, the flatness of the energy bands induced by the Rashba effect makes them promising candidates for further realizing the integer or fractional QAH effect. With tunable Rashba intensity, interlayer coupling, and twist angle, this work positions Rashba materials as a versatile platform for exploring and controlling topological properties.

5. Experimental Section

First-Principle Calculations: The first-principles simulations are performed using the Vienna ab initio Simulation Package (VASP).[64] The atomic structure optimization is performed within the generalized gradient approximation (GGA) and Perdew–Burke–Ernzerhof (PBE) exchange-correlation functional until the force on each atom is less than 0.02 eV/Å.[65,66] The electronic iteration convergence criterion is set to 1×10^{-6} eV. To avoid spurious interactions between periodic images, a vacuum space of at least 20 Å is introduced. The k-mesh is set to 11 × 11 × 1 with a 450-eV cutoff energy. Dipole moment correction is employed,[67] and the DFT-D3 method is employed to include vdW interactions.[68] The lattice parameters of the bulk BiTeI material were calculated with different vdW corrections, and compared to experimental results, as shown in Table S3 (Supporting Information). It was found that the D_3 correction yielded results most consistent with experiments. Therefore, the D_3 vdW correction was chosen for the first-principles calculations and for fitting the continuum model. Spin-orbit coupling (SOC) is included in the total energy calculations.

Supporting Information

Supporting Information is available from the Wiley Online Library or from the author.

Acknowledgements

X.X. and H.W. contributed equally to this work. X.X. is supported by the National Science Foundation (NSF) Designing Materials to Revolutionize and Engineer our Future (DMREF) DMR-2118779. L.Y. is supported by NSF DMR- 2124934. The simulation used Anvil at Purdue University through allocation DMR100005 from the Advanced Cyberinfrastructure Coordination Ecosystem: Services & Support (ACCESS) program, which is supported by National Science Foundation grants #2138259, #2138286, #2138307, #2137603, and #2138296.

Conflict of Interest

The authors declare no conflict of interest.

Data Availability Statement

The data that support the findings of this study are available in the supplementary material of this article.

Keywords

first-principles calculations, moiré system, topological flat bands, twisted bilayer, type-II Rashba

Received: December 23, 2024
Revised: April 15, 2025

---

[1] D. Leykam, A. Andreanov, S. Flach, *Adv. Phys.: X* **2018**, *3*, 1473052.
[2] Z. Jiang, Z. Liu, H. Ma, W. Xia, Z. Liu, J. Liu, S. Cho, Y. Yang, J. Ding, J. Liu, Z. Huang, Y. Qiao, J. Shen, W. Jing, X. Liu, J. Liu, Y. Guo, D. Shen, *Nat. Commun.* **2023**, *14*, 4892.
[3] Y. Hu, C. Le, Y. Zhang, Z. Zhao, J. Liu, J. Ma, N. C. Plumb, M. Radovic, H. Chen, A. P. Schnyder, X. Wu, X. Dong, J. Hu, H. Yang, H.-J. Gao, M. Shi, *Nat. Phys.* **2023**, *19*, 1827.
[4] Z. Zhang, Y. Wang, K. Watanabe, T. Taniguchi, K. Ueno, E. Tutuc, B. J. LeRoy, *Nat. Phys.* **2020**, *16*, 1093.
[5] L. Balents, C. R. Dean, D. K. Efetov, A. F. Young, *Nat. Phys.* **2020**, *16*, 725.
[6] J. Mao, S. P. Milovanovic, M. Andelkovic, X. Lai, Y. Cao, K. Watanabe, T. Taniguchi, L. Covaci, F. M. Peeters, A. K. Geim, Y. Jiang, E. Y. Andrei, *Nature* **2020**, *584*, 215.
[7] M. Levin, A. Stern, *Phys. Rev. Lett.* **2009**, *103*, 196803.
[8] D. N. Sheng, Z.-C. Gu, K. Sun, L. Sheng, *Nat. Commun.* **2011**, *2*, 389.
[9] T. Neupert, L. Santos, C. Chamon, C. Mudry, *Phys. Rev. Lett.* **2011**, *106*, 236804.
[10] N. Regnault, B. A. Bernevig, *Phys. Rev. X* **2011**, *1*, 021014.
[11] E. Tang, J.-W. Mei, X.-G. Wen, *Phys. Rev. Lett.* **2011**, *106*, 236802.
[12] C. Wang, L. Gioia, A. A. Burkov, *Phys. Rev. Lett.* **2020**, *124*, 096603.
[13] E. M. Spanton, A. A. Zibrov, H. Zhou, T. Taniguchi, K. Watanabe, M. P. Zaletel, A. F. Young, *Science* **2018**, *360*, 62.
[14] H. Park, J. Cai, E. Anderson, Y. Zhang, J. Zhu, X. Liu, C. Wang, W. Holtzmann, C. Hu, Z. Liu, T. Taniguchi, K. Watanabe, J.-H. Chu, T. Cao, L. Fu, W. Yao, C.-Z. Chang, D. Cobden, D. Xiao, X. Xu, *Nature* **2023**, *622*, 74.
[15] J. Cai, E. Anderson, C. Wang, X. Zhang, X. Liu, W. Holtzmann, Y. Zhang, F. Fan, T. Taniguchi, K. Watanabe, Y. Ran, T. Cao, L. Fu, D. Xiao, W. Yao, X. Xu, *Nature* **2023**, *622*, 63.
[16] Z. Lu, T. Han, Y. Yao, A. P. Reddy, J. Yang, J. Seo, K. Watanabe, T. Taniguchi, L. Fu, L. Ju, *Nature* **2024**, *626*, 759.
[17] F. Xu, Z. Sun, T. Jia, C. Liu, C. Xu, C. Li, Y. Gu, K. Watanabe, T. Taniguchi, B. Tong, J. Jia, Z. Shi, S. Jiang, Y. Zhang, X. Liu, T. Li, *Phys. Rev. X* **2023**, *13*, 031037.
[18] C. Wang, X.-W. Zhang, X. Liu, Y. He, X. Xu, Y. Ran, T. Cao, D. Xiao, *Phys. Rev. Lett.* **2024**, *132*, 036501.
[19] X. Liu, Y. He, C. Wang, X.-W. Zhang, T. Cao, D. Xiao, *Phys. Rev. Lett.* **2024**, *132*, 146401.
[20] A. P. Reddy, F. Alsallom, Y. Zhang, T. Devakul, L. Fu, *Phys. Rev. B* **2023**, *108*, 085117.
[21] C. Xu, J. Li, Y. Xu, Z. Bi, Y. Zhang, *Proc. Natl. Acad. Sci. USA* **2024**, *121*, 2316749121.
[22] T. Devakul, V. Crépel, Y. Zhang, L. Fu, *Nat. Commun.* **2021**, *12*, 6730.
[23] M. Claassen, L. Xian, D. M. Kennes, A. Rubio, *Nat. Commun.* **2022**, *13*, 4915.
[24] Y. Zhang, T. Devakul, L. Fu, *Proc. Natl. Acad. Sci. USA* **2021**, *118*, 2112673118.
[25] F. Wu, T. Lovorn, E. Tutuc, A. H. MacDonald, *Phys. Rev. Lett.* **2018**, *121*, 026402.
[26] F. Wu, T. Lovorn, E. Tutuc, I. Martin, A. H. MacDonald, *Phys. Rev. Lett.* **2019**, *122*, 086402.
[27] G. Bihlmayer, P. Noël, D. V. Vyalikh, E. V. Chulkov, A. Manchon, *Nat. Rev. Phys.* **2022**, *4*, 642.
[28] Y. A. Bychkov, E. I. Rashba, *J. Phys. C: Solid State Phys.* **1984**, *17*, 6039.
[29] S. Lee, H. Koike, M. Goto, S. Miwa, Y. Suzuki, N. Yamashita, R. Ohshima, E. Shigematsu, Y. Ando, M. Shiraishi, *Nat. Mater.* **2021**, *20*, 1228.
[30] K. Miyata, X. Y. Zhu, *Nat. Mater.* **2018**, *17*, 379.
[31] S. D. Ganichev, V. V. Bel'kov, L. E. Golub, E. L. Ivchenko, P. Schneider, S. Giglberger, J. Eroms, J. De Boeck, G. Borghs, W. Wegscheider, D. Weiss, W. Prettl, *Phys. Rev. Lett.* **2004**, *92*, 256601.
[32] H. Nakamura, T. Koga, T. Kimura, *Phys. Rev. Lett.* **2012**, *108*, 206601.
[33] G. Bihlmayer, O. Rader, R. Winkler, *New J. Phys.* **2015**, *17*, 050202.
[34] X. Zhang, Q. Liu, J. W. Luo, A. J. Freeman, A. Zunger, *Nat. Phys.* **2014**, *10*, 387.
[35] S. Lee, M. Kim, Y. K. Kwon, *npj 2D Mater. Appl.* **2023**, *7*, 43.
[36] G. Gatti, D. Gosálbez-Martínez, S. Roth, M. Fanciulli, M. Zacchigna, M. Kalläne, K. Rossnagel, C. Jozwiak, A. Bostwick, E. Rotenberg, A. Magrez, H. Berger, I. Vobornik, J. Fujii, O. V. Yazyev, M. Grioni, A. Crepaldi, *Commun. Phys.* **2021**, *4*, 54.
[37] L. Yuan, Q. Liu, X. Zhang, J. W. Luo, S. S. Li, A. Zunger, *Nat. Commun.* **2019**, *10*, 906.
[38] M. S. Bahramy, R. Arita, N. Nagaosa, *Phys. Rev. B* **2011**, *84*, 041202.
[39] K. Ishizaka, M. S. Bahramy, H. Murakawa, M. Sakano, T. Shimojima, T. Sonobe, K. Koizumi, S. Shin, H. Miyahara, A. Kimura, K. Miyamoto, T. Okuda, H. Namatame, M. Taniguchi, R. Arita, N. Nagaosa, K. Kobayashi, Y. Murakami, R. Kumai, Y. Kaneko, Y. Onose, Y. Tokura, *Nat. Mater.* **2010**, *10*, 521.
[40] A. Crepaldi, L. Moreschini, G. Autès, C. Tournier-Colletta, S. Moser, N. Virk, H. Berger, Ph. Bugnon, Y. J. Chang, K. Kern, A. Bostwick, E. Rotenberg, O. V. Yazyev, M. Grioni, *Phys. Rev. Lett.* **2012**, *109*, 096803.
[41] G. Bianca, C. Trovatello, A. Zilli, M. I. Zappia, S. Bellani, N. Curreli, I. Conticello, J. Buha, M. Piccinni, M. Ghini, M. Celebrano, M. Finazzi, I. Kriegel, N. Antonatos, Z. Sofer, F. Bonaccorso, *ACS Appl. Mater. Interfaces* **2022**, *14*, 34963.
[42] N. Antonatos, E. Kovalska, V. Mazánek, M. Veselý, D. Sedmidubský, B. Wu, Z. Sofer, *ACS Appl. Nano Mater.* **2021**, *4*, 590.
[43] H. Maaß, H. Bentmann, C. Seibel, C. Tusche, S. V. Eremeev, T. R. F. Peixoto, O. E. Tereshchenko, *Nat. Commun.* **2016**, *7*, 11621.
[44] J. S. Lee, G. A. H. Schober, M. S. Bahramy, H. Murakawa, Y. Onose, R. Arita, N. Nagaosa, Y. Tokura, *Phys. Rev. Lett.* **2011**, *107*, 117401.
[45] C. M. Acosta, E. Ogoshi, A. Fazzio, G. M. Dalpian, A. Zunger, *Matter* **2020**, *3*, 145.
[46] G. Yu, L. Wen, G. Luo, Y. Wang, *Phys. Scr.* **2021**, *96*, 125874.
[47] H. Rostami, F. Guinea, M. Polini, R. Roldán, *npj 2D Mater. Appl.* **2018**, *2*, 15.
[48] F. Zhang, A. H. MacDonald, E. J. Mele, *Proc. Natl. Acad. Sci. USA* **2013**, *110*, 10546.
[49] S. Sinha, P. C. Adak, R. S. Surya Kanthi, B. L. Chittari, L. D. V. Sangani, K. Watanabe, T. Taniguchi, J. Jung, M. M. Deshmukh, *Nat. Commun.* **2020**, *11*, 5548.
[50] C. Ma, Q. Wang, S. Mills, X. Chen, B. Deng, S. Yuan, C. Li, K. Watanabe, T. Taniguchi, X. Du, F. Zhang, F. Xia, *Nano Lett.* **2020**, *20*, 6076.
[51] J. Lee, K. F. Mak, J. Shan, *Nat. Nanotechnol.* **2016**, *11*, 421.
[52] S. O. Valenzuela, M. Tinkham, *Nature* **2006**, *442*, 176.
[53] W.-X. Qiu, B. Li, X.-J. Luo, F. Wu, *Phys. Rev. X* **2023**, *13*, 041026.
[54] X.-W. Zhang, C. Wang, X. Liu, Y. Fan, T. Cao, D. Xiao, *Nat. Commun.* **2024**, *15*, 4223.
[55] C. L. Kane, E. J. Mele, *Phys. Rev. Lett.* **2005**, *95*, 146802.
[56] C. L. Kane, E. J. Mele, *Phys. Rev. Lett.* **2005**, *95*, 226801.
[57] Z. Liu, H. Wang, J. Wang, *Phys. Rev. B* **2022**, *106*, 035114.
[58] H. Wang, L. Yang, *Phys. Rev. B* **2023**, *107*, 235427.
[59] R. Yu, W. Zhang, H.-J. Zhang, S.-C. Zhang, X. Dai, Z. Fang, *Science* **2010**, *329*, 61.

[60] C.-Z. Chang, J. Zhang, X. Feng, J. Shen, Z. Zhang, M. Guo, K. Li, Y. Ou, P. Wei, L.-L. Wang, Z.-Q. Ji, Y. Feng, S. Ji, X. Chen, J. Jia, X. Dai, Z. Fang, S.-C. Zhang, K. He, Y. Wang, L. Lu, X.-C. Ma, Q.-K. Xue, *Science* **2013**, *340*, 167.
[61] T. Li, S. Jiang, B. Shen, Y. Zhang, L. Li, Z. Tao, T. Devakul, K. Watanabe, T. Taniguchi, L. Fu, J. Shan, K. F. Mak, *Nature* **2021**, *600*, 641.
[62] C. Liu, H. Gao, Y. Li, K. Wang, L. A. Burton, W. Ren, *J. Mater. Chem. C* **2020**, *8*, 5143.
[63] P. Z. Hanakata, A. S. Rodin, A. Carvalho, H. S. Park, D. K. Campbell, A. H. Castro Neto, *Phys. Rev. B* **2017**, *96*, 161401.
[64] G. Kresse, J. Furthmüller, *Phys. Rev. B* **1996**, *54*, 11169.
[65] J. P. Perdew, K. Burke, M. Ernzerhof, *Phys. Rev. Lett.* **1996**, *77*, 3865.
[66] G. Kresse, D. Joubert, *Phys. Rev. B* **1999**, *59*, 1758.
[67] J. Neugebauer, M. Scheffler, *Phys. Rev. B* **1992**, *46*, 16067.
[68] S. Grimme, S. Ehrlich, L. Goerigk, *J. Comput. Chem.* **2011**, *32*, 1456.